Local water slamming of curved rigid hulls

J. Xiao and R. C. Batra*
Department of Engineering Science and Mechanics
Virginia Polytechnic Institute and State University
Blacksburg, VA 24061

ABSTRACT

We use the boundary element method (BEM) to study transient plane strain deformations of water induced by a rigid hull impacting at normal incidence initially stationary water occupying a half space with the goal of finding the hydrodynamic pressure acting on the hull. Water is assumed to be incompressible and inviscid, and its deformations to have zero vorticity. Thus deformations of water are governed by the Laplace equation. Challenging issues addressed are finding the free surface of water whose evolution is governed by a nonlinear partial differential equation, determining the *a priori* unknown wetted length, and ensuring that water maintains contact with the hull without penetrating into it. The solution of the problem using the commercial software, LSDYNA, resulted in water penetrating into a rigid hull. The developed BEM code has been verified by using the method of manufactured solutions. Computed results for the hydrostatic pressure on straight hulls and ship bow section are found to compare well with the corresponding experimental findings. It is found that the peak pressure acting near the terminus of the wetted length decreases with an increase in the radius of the circular hull.

Keywords: Water slamming, curved hulls, ship bow section.

1. INTRODUCTION

Local water slamming is characterized by large hydrodynamic loads of short duration which can cause significant structural damage, e.g., see Faltinsen [1]. The water entry of a rigid V-shaped wedge of small deadrise angle β was first studied by von Kármán [2]. Subsequently, Wagner [3] generalized von Kármán's work by including effects of water splash-up on the body. Similarity solutions for water slamming of a rigid wedge were developed by Dobrovol'skaya [4] for β greater than 30° and by Zhao and Faltinsen [5] for 4° ≤ β ≤ 81°. Zhao et al. [6] generalized Wagner's solution for arbitrary values of β and numerically solved the problem using the boundary integral method. Effects of jet flow were neglected and computed results were found to agree with the corresponding experimental findings. Mei et al. [7] analytically and numerically solved the two-dimensional water impact problem for wedges and circular cylinders including effects of jet flow. Yettou et al. [8] experimentally measured hydrodynamic pressures acting on rigid wedges during their free fall into stationary water and also analytically solved the problem.

Fluid motions of water entry problems have been simulated by several numerical techniques such as the finite element method (FEM) [9], the FEM with Arbitrary-Lagrangian-Eulerian (ALE) formulation [10], smoothed particle hydrodynamics (SPH)

*Corresponding author, E-mail: rbatra@vt.edu, Tel. +1-540-231-6051

method [11] and the boundary element method (BEM) [5], [12], [13]. Zhao and Faltinsen [5] analyzed the water entry of a rigid wedge using the BEM and compared computed results with those obtained by the similarity method. Lin and Ho [12] used the BEM to study the influence of water depth on the slamming pressure acting on a rigid wedge. They found that the maximum impact pressure is larger for shallow water than that for deep water which agreed with their experimental observations. Battistin and Iafrati [13] used the BEM to simulate two-dimensional water entry problems of arbitrary shaped bodies.

In practical water slamming problems, the hull is curved and deformable. Hull's deformations affect the motion of the fluid and the hydroelastic pressure acting on the solid-fluid interface. Sun [14] and Sun and Faltinsen [15, 16] numerically analyzed water slamming problems for arbitrary geometries using the BEM for studying deformations of water that was modeled as non-viscous and incompressible, and modal analysis for deformations of the cylindrical shell. They considered effects of gravity and flow separation from the solid surface. Qin and Batra [17] studied the hydroelastic problem using {3, 2}-order plate theory for a sandwich hull of small deadrise angle and modified Wagner's water impact theory to consider the fluid-structure interaction during slamming. The plate theory incorporates the transverse shear and the transverse normal deformations of the core, but not of the face sheets which were modeled as Kirchhoff plates. Das and Batra [18] studied the water slamming of deformable sandwich hulls using the commercial FE software LSDYNA with the ALE formulation. They considered all geometric nonlinearities when studying hull's deformations, assumed the fluid to be compressible, accounted for inertia effects in the fluid and the solid, and examined delamination between the core and the face sheets. They pointed out that boundary conditions at the fluid/solid interface were not well satisfied since the fluid penetrated into the rigid hull. Stenius et al. [19] used LSDYNA to study hydroelastic effects for deformable hulls considering different boundary conditions, impact velocities, deadrise angles, membrane effects and hull materials. Lu et al. [20] employed the coupled BEM and the FEM for studying hydroelastic effects with the hull modeled as a Timoshenko beam. Panciroli et al. [21] experimentally and numerically analyzed the water slamming of linear elastic wedges. The experimental results for different values of the panel thickness, deadrise angle and entry velocity were compared with those obtained by using the SPH formulation in LSDYNA. Oger et al. [11] used twenty million particles to correctly predict the pressure on the wedge. Experimental results for the failure of deformable sandwich composite panels including core shear, delamination and damage of the face sheets due to water slamming are reported in [22, 23]. Hu et al. [24] approximated the slamming pressure by equivalent bending moment to study delamination of a composite hull using the FE software ANSYS and the cohesive zone model. Water slamming problem for a composite hull of a rather complex shape has been analyzed by Paepegem et al. [25] both numerically using ABAQUS and experimentally. Aureli et al. [26] have exploited deformations due to fluid structure interaction to harvest energy.

We focus here on delineating the effect of hull curvature on pressure acting on the hull. Even though hulls deform due to water slamming loads and the maximum hydrodynamic pressures acting on rigid and deformable hulls may be different, estimates of the maximum pressure on rigid hulls will provide useful guidelines for designers.

2. PROBLEM FORMULATION

A schematic sketch of the problem studied is shown in Fig. 1. At time $t = 0$, the ship hull keel impacts at normal incidence with vertically downward velocity V stationary water occupying the semi-infinite domain $Z \leq 0$ when rectangular Cartesian coordinates (X, Y, Z) fixed to the earth are used to describe deformations of the fluid. We simplify the problem by assuming

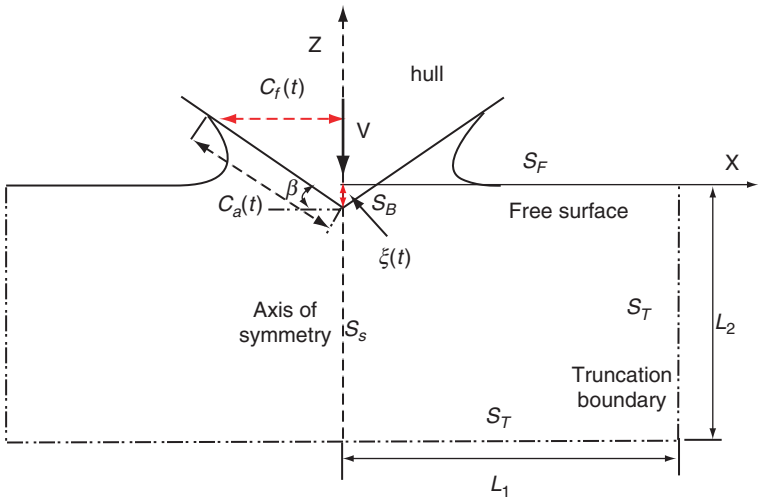

Figure 1 Schematic sketch of the water slamming problem studied.

that the hull dimensions in the Y-direction are very large so that a plane strain state of deformation in the XZ-plane can be assumed and the problem can be solved as 2-dimensional (2-D). Furthermore, we assume that the hull geometry is symmetric about the plane $X = 0$ and it initially impacts water along the line $X = Z = 0$. Thus deformations of water in the region $X \geq 0$ and $Z \leq 0$ and motion of the right-half of the hull are analyzed.

We note that the hydrodynamic load acting on the hull is highly localized; thus the slamming problem is idealized as that of either straight or curved wedge entering water with a vertically downward speed (see Fig. 1) that may change due to the force exerted by water on the hull and the consideration of gravity forces. Even though gravity and surface tension effects are not considered in studying deformations of water, the analysis could be modified to account for gravitational forces. We derive equations governing deformations of water using balance laws of mass, linear momentum and moment of momentum, and the continuity of velocity and surface tractions at the hull/water interface. Sources of nonlinearities include (i) the *a priori* unknown length of the wetted surface, (ii) dependence of pressure at a point on the square of the velocity potential gradient, and (iii) the *a priori* unknown deformed shape of the free surface of water. Both the wetted length and the shape of the free surface of water are to be determined as a part of the solution of the problem.

2.1. EQUATIONS GOVERNING DEFORMATIONS OF THE FLUID

For hull speeds of the order of 10 m/s, viscous effects in water are often neglected. Also, the time duration during which the compressibility of water likely plays a noticeable role is considerably smaller than that of interest in the water slamming problem. We thus assume the water to be incompressible, homogeneous and inviscid and its deformations to be irrotational. The assumption of null vorticity implies that there exists a velocity potential φ such that velocity $\boldsymbol{v} = -\nabla\varphi$, where ∇ is the spatial gradient operator in the XZ-plane. The assumption of incompressibility requires that φ satisfy the Laplace equation:

$$\frac{\partial^2\varphi}{\partial Z^2} + \frac{\partial^2\varphi}{\partial X^2} = 0 \text{ , in the water domain.} \tag{1}$$

Eq. (1) expresses the balance of mass. In the absence of gravity force, the balance of linear momentum for an inviscid fluid gives

$$\rho \frac{D\boldsymbol{v}}{Dt} = -\nabla p, \tag{2}$$

where ρ is the mass density of water, D/Dt is the total time derivative, and the hydrostatic pressure p is determined by solving Eq. (2) under the following boundary conditions.

$$p = p_a, \frac{DX}{Dt} = -\frac{\partial \varphi}{\partial X}, \frac{DZ}{Dt} = -\frac{\partial \varphi}{\partial Z}, \quad \frac{D\varphi}{Dt} = -\frac{1}{2}|\nabla \varphi|^2 \quad \text{on the free surface of water,} \tag{3.a}$$

$$|v| \to 0 \text{ as } (X^2 + Z^2)^{1/2} \to \infty \text{ for } X > 0 \text{ and } Z \le 0, \tag{3.b}$$

$$\frac{\partial \varphi}{\partial X} = 0 \quad \text{on } X = 0. \tag{3.c}$$

Here p_a is the atmospheric pressure. In writing boundary condition (3.a) we have tacitly neglected the surface tension effect. These equations imply that the velocity of a point on the free surface equals that of the fluid particle instantaneously occupying it. Eq. $(3.a)_4$ following from Eq. $(3.a)_1$ and the Bernoulli Eq. (5) is used to update the function φ on the free surface after every time step. Ideally one should specify in Eq. (3.b) the rate of decay of the speed of water at infinity. However, we do not do so since the domain occupied by the fluid will be truncated to a finite one when numerically solving the problem. The boundary condition (3.c) follows from the assumption that deformations are symmetric about the plane $X = 0$. At the fluid/hull interface the non-penetration of the fluid into the solid is satisfied if

$$\frac{\partial \varphi}{\partial n} = -\boldsymbol{V} \cdot \boldsymbol{n} \tag{4}$$

where $\boldsymbol{V}$ is velocity of the hull particle and $\boldsymbol{n}$ is a unit vector normal to the fluid/hull interface (pointing into hull).

We note that Eqs. (1) – (4) for finding p and v are coupled, Eq. $(3.a)_4$ is nonlinear in φ, and the free surface of water and the wetted surface of hull are to be determined as parts of the solution of the problem.

Recalling that $v = -\nabla \varphi$, Eq. (2) can be integrated to give the following Bernoulli equation:

$$p - p_a = -\rho\left(-\frac{\partial \varphi}{\partial t} + \frac{1}{2}|\nabla \varphi|^2\right). \tag{5}$$

2.2. NUMERICAL SOLUTION OF THE PROBLEM

2.2.1. Analysis of fluid's deformations by the BEM

We use the BEM to solve Laplace Eq. (1) and truncate the domain occupied by the fluid to lengths L_1 and L_2 in the X- and Z- directions, respectively (cf. Fig. 1). Values of L_1 and L_2 will be determined iteratively to compute a converged solution near the hull/water interface.

Using Green's second identity, the velocity potential at point j in the fluid (either in the interior or on the boundary) can be written as [27] :

$$c(j)\varphi(j) = \int_{\partial\Omega} G(\boldsymbol{\xi}, j)\frac{\partial\varphi(\boldsymbol{\xi})}{\partial n}ds(\boldsymbol{\xi}) - \int_{\partial\Omega}\varphi(\boldsymbol{\xi})\frac{\partial G(\boldsymbol{\xi}, j)}{\partial n}ds(\boldsymbol{\xi}) , \tag{6}$$

where $G(\boldsymbol{\xi}, j)$, = ln $r(\boldsymbol{\xi}, j)$, $r(\boldsymbol{\xi}, j)$ is the distance between source point ξ on the fluid boundary and point j, $c(j)$ is a constant, $\boldsymbol{n}$ is a unit normal pointing out of the fluid domain, and Ω equals the region occupied by the fluid. We note that c, φ, Ω and $\boldsymbol{n}$ vary with time t; this dependence is not exhibited to simplify the notation. Since Eq. (6) holds even when the velocity potential is a constant, we get

$$c(j) = -\int_{\partial\Omega}\frac{\partial G(\boldsymbol{\xi}, j)}{\partial n}ds(\boldsymbol{\xi}), \tag{7}$$

The integral Eq. (6) is converted into a system of simultaneous linear algebraic equations by using piecewise linear basis functions, i.e., the boundary of the fluid domain is discretized by using 2-node 1-D elements. Since $G(\boldsymbol{\xi}, j)$ = ln $r(\boldsymbol{\xi}, j)$ the integrals in Eq. (6) are numerically evaluated by using 6 Gauss points in each element. Thus Eq. (6) can be written as

$$[H]\begin{Bmatrix}\varphi^F\\ \varphi^B\\ \varphi^{T+S}\end{Bmatrix} = [G]\begin{Bmatrix}\dfrac{\partial\varphi}{\partial n}^F\\ \dfrac{\partial\varphi}{\partial n}^B\\ \dfrac{\partial\varphi}{\partial n}^{T+S}\end{Bmatrix}, \tag{8}$$

where elements of matrices $[H]$ and $[G]$ depend upon coordinates of nodes, and superscripts F, B, T and S on a quantity represent, respectively, its value at a node on the free surface, the hull/water interface, the truncation boundaries and the axis of symmetry.

Recalling that at time t we know at every point on the fluid boundary either φ or $\dfrac{\partial\varphi}{\partial n}$ we can solve for the other variable at that point. Transforming unknowns in Eq. (8) to the left hand side, we rewrite Eq. (8) as

$$[A]\begin{Bmatrix}\dfrac{\partial\varphi}{\partial n}^F\\ \varphi^B\\ \varphi^{T+S}\end{Bmatrix} = [B]\begin{Bmatrix}\varphi^F\\ \dfrac{\partial\varphi}{\partial n}^B\\ \dfrac{\partial\varphi}{\partial n}^{T+S}\end{Bmatrix}. \tag{9}$$

In writing Eq. (9) we have used boundary conditions listed in Eq. (4) and taken the velocity of hull particles to be known.

After having solved Eq. (9) we know φ and $\frac{\partial \varphi}{\partial n}$ at every point on the fluid boundary at time t. Thus the tangential derivative $\frac{\partial \varphi}{\partial s}$ of φ at points on the boundary $\partial\Omega$ can be computed; here s is the arc length along $\partial\Omega$. Combining $\frac{\partial \varphi}{\partial s}$ with the computed $\frac{\partial \varphi}{\partial n}$ on $\partial\Omega$, the gradient vector $\nabla\varphi$ at points on the hull/water interface and on the free surface of water is determined, and the free surface profile, and values of φ at points on the free surface are updated using Eq. (3.a). Eq. (6) is used to determine the velocity potential φ at any point in the fluid domain.

We need to determine $\frac{\partial \varphi}{\partial t}$ to obtain the pressure field in the fluid domain from Eq. (5). It is found by introducing a new variable Ψ defined by

$$\Psi = \frac{\partial \varphi}{\partial t} + \boldsymbol{V} \cdot \nabla \varphi \ . \tag{10}$$

It has been proved by Greco [28] that Ψ also satisfies the 2-D Laplace equation

$$\frac{\partial^2 \Psi}{\partial X^2} + \frac{\partial^2 \Psi}{\partial Z^2} = 0 \ . \tag{11}$$

Following Sun [14] and deferring details to the Appendix, boundary conditions for Ψ are

$$\Psi = \boldsymbol{V} \cdot \nabla \varphi + \frac{1}{2} \left| \nabla \varphi \right|^2 \quad \text{on the free surface,} \tag{12.a}$$

$$\frac{\partial \Psi}{\partial n} = -\boldsymbol{n} \cdot \dot{\boldsymbol{V}} \quad \text{on the solid body/fluid interface,} \tag{12.b}$$

$$\frac{\partial \Psi}{\partial n} = 0 \quad \text{on the axis of symmetry and on truncation boundaries.} \tag{12.c}$$

Here $\dot{\boldsymbol{V}}$ is the acceleration of the rigid body motion of particles on the hull surface.

At every time t, the boundary value problem defined by Eqs. (11) and (12) is numerically solved by the BEM. The algebraic equation for the determination of Ψ and $\frac{\partial \Psi}{\partial n}$ at boundary points is

$$[A] \begin{Bmatrix} \dfrac{\partial \Psi^F}{\partial n} \\ \Psi^B \\ \Psi^{T+S} \end{Bmatrix} = [B] \begin{Bmatrix} \Psi^F \\ \dfrac{\partial \Psi^B}{\partial n} \\ \dfrac{\partial \Psi^{T+S}}{\partial n} \end{Bmatrix}, \tag{13}$$

where matrices [A] and [B] are the same as those in Eq. (9). Knowing Ψ and φ, from Eq. (10) $\frac{\partial \varphi}{\partial t}$ can be evaluated at all points on the fluid boundary including those on the fluid/solid interface. This approach avoids finding $\frac{\partial \varphi}{\partial t}$ by the backward difference method at the computational cost of solving twice the boundary value problem for the fluid. Recall that the value of φ at any point in the fluid domain is found from Eqs. (6) and (7).

2.2.2. Analysis of the motion of free surface of water

The free surface of stationary water changes rapidly when a solid body enters it at time $t = 0$. For small values of time t Sun [14] proposed that the free surface profile for the water entry of a straight solid body can be approximated by

$$Z(t) = \frac{X\xi(t)}{c_f(t)} \arcsin\left(\frac{c_f(t)}{X}\right) - \xi(t) \quad \text{for} \quad X > c_f(t) \tag{14}$$

where $\xi(t)$ is the submergence of the solid body apex relative to the undisturbed free surface,

$$c_f(t) = \frac{\pi\xi(t)}{2\tan\beta}, \tag{15}$$

is the absolute value of X-coordinate of jet tip, and β is the deadrise angle; $\xi(t)$ and $c_f(t)$ are shown in Fig. 1. Eq. (15) is Wagner's [3] approximation and is generally valid for small values of β.

For water slamming of a circular hull with the deadrise angle at $X = 0$ not equal to zero, we assume that the hull region close to the apex can be regarded as straight and approximate the free surface of water near the apex using Eq. (14). For an arbitrary shaped hull with deadrise angle at $X = 0$ equal to zero, we assume that the free surface of water is undisturbed for the first time step. The velocity potential on the free surface is assumed to be zero at the initial time. Assuming that the downward velocity at the apex of the hull will not change during a short period of time, the first time step size, δt, is obtained from Eq. (14) with $c_f(\delta t) = 0.005\ \mathcal{L}$ where $\mathcal{L}$ is the hull arc length, and $\xi(\delta t) = V\delta t$.

A very thin jet in the water surface is generally formed where water separates from the solid hull surface. Capturing this jet is computationally expensive. One way to alleviate this problem is to truncate the jet. For example, Zhao and Faltinsen [5] as well as Battistin and Iafrati [13] accomplish this by putting an element perpendicular to the wedge when the angle between the water surface and the wedge is smaller than a threshold value. This usually results in oscillatory pressure distribution on the wedge. As shown in Fig. 2a, Sun [14] introduced a new segment on the free surface when the jet became too thin, i.e., when distance from point B to the solid body becomes smaller than a threshold value d_0, the point is projected on the wedge and a new segment CD replaces the free water surface CA. Point B is found by starting from a point away from the jet tip, and evaluating the distance of this point from the hull. Point B is the first node on the free surface of water whose distance from the hull is less than the threshold value d_0. We note that Sun [16] did not elaborate upon the method to find point B. This method reduces oscillations in the pressure distribution on the hull; we name this approach of truncating the jet as "distance cut method". We adopt a

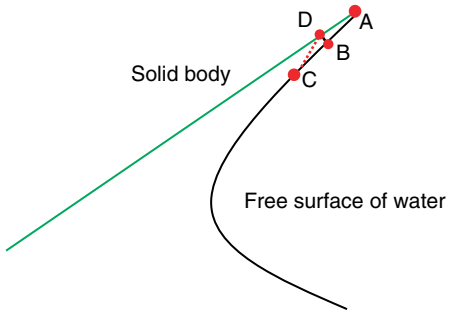

(a) Distance cut method for truncating a thin jet

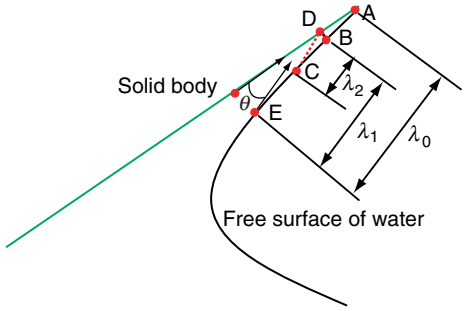

(b) Angle cut method for truncating a thin jet ($\lambda_1 = 0.8\lambda_0$, $\lambda_2 = 0.1\,\lambda_0$)

Figure 2 Two techniques for truncating a thin jet.

similar method and call it "angle cut method". Referring to Fig. 2b, we find the tangent at every point of the free surface of water and the tangent at the corresponding point to the solid body surface. The angle θ between the two tangents at the abutting points of the fluid and the solid is calculated. Starting from the jet tip A, we find the first point E on the jet surface for which θ is larger than the threshold value θ_0. When the length between points E and A becomes more than the jet cut threshold length λ_0, point B is projected on the wedge to point D. λ_0 is equal to $0.1\mathcal{L}$ in present study and $\mathcal{L}$ is the arc length of the hull. The length between points E and B is called the jet keep length λ_1 and it is taken to equal $0.8\lambda_0$. Point C on the jet is selected such that length CB, called the jet smoothing length λ_2 equals $0.1\lambda_0$. A new section CD replaces CA and values of the velocity potential at points on CD are derived by interpolating and extrapolating from those on the section CB. Battistin and Iafrati [13] suggested that the threshold angle, θ_0, should be between 4° and 10° depending upon the hull shape; here we take $\theta_0 = 4°$. Thus we first find the jet starting point E as described above, and then locate points B and C according to the values of the jet keep length and the jet smoothing length, respectively, point D is the projection of point B onto the solid body.

Even with the truncating of a thin jet the numerical solution becomes unstable due to the free surface profile becoming non-smooth after the solution has been computed for several time steps. Many smoothing methods have been proposed to remove the saw-tooth instability in the free surface. We smooth the $X-$ and $Z-$ coordinates and the velocity potential φ using the smooth function defined in Longuet and Cokelet [29]. A function $\mathcal{F}(s)$ defined at points s_j (j = 1, 2,…, N) can be locally approximated by the function

$$f(s) = (a_0 + a_1 s + a_2 s^2) + (-1)^j \, (b_0 + b_1 s) \,. \tag{16}$$

Here s is the arc length along the water surface, and a_0, a_1…, b_0, b_1… are coefficients which can be chosen uniquely by setting $f(s) = \mathcal{F}(s)$ at nodes s_{j-2}, s_{j-1}, s_j, s_{j+1}, and s_{j+2} when $j = 3, 4, \ldots, N-2$. These coefficients for end nodes $j = 1, 2$ and $j = N, N-1$ can be evaluated uniquely by setting $f(s) = \mathcal{F}(s)$ at the first and the last 5 nodes, respectively. Terms in the first parentheses in Eq. (16) give the smoothed mean curve, and those in the second parentheses represent oscillations in the data. Omitting terms in the second parentheses we get the smooth function

$$\bar{f}(s) = a_0 + a_1 s + a_2 s^2 \tag{17}$$

as the approximation of $\mathcal{F}(s)$.

Assuming the nodes are uniformly distributed when $j = 1, 2, N-1, N$, and non-uniformly distributed for other values of j, the five-point smoothing function can be written as

$$\bar{f}_1 = \frac{11 f_1 + 12 f_2 - 6 f_3 - 4 f_4 + 3 f_5}{16} \,, \tag{18.a}$$

$$\bar{f}_2 = \frac{3 f_1 + 8 f_2 + 6 f_3 - f_5}{16} \,, \tag{18.b}$$

$$\bar{f}_j = c_{j-2} f_{j-2} + c_{j-1} f_{j-1} + c_j f_j + c_{j+1} f_{j+1} + c_{j+2} f_{j+2} \,, \tag{18.c}$$

$$\bar{f}_{N-1} = \frac{3 f_N + 8 f_{N-1} + 6 f_{N-2} - f_{N-4}}{16} \,, \tag{18.d}$$

$$\bar{f}_N = \frac{11 f_N + 12 f_{N-1} - 6 f_{N-2} - 4 f_{N-3} + 3 f_{N-4}}{16} \,, \tag{18.e}$$

where

$$c_{j-2} = -\frac{h_j h_{j-1}}{2(h_{j-1} + h_{j-2})(h_{j-1} + h_{j-2} + h_j + h_{j+1})}, \quad c_{j-1} = \frac{h_j}{2(h_{j-1} + h_j)},$$
$$c_j = \frac{(h_{j-1} + h_{j-2})(2h_j + h_{j+1}) - h_j h_{j-2}}{2(h_{j-1} + h_{j-2})(h_j + h_{j+1})}, \quad c_{j+1} = \frac{h_{j-1}}{2(h_{j-1} + h_j)},$$
$$c_{j+2} = -\frac{h_j h_{j-1}}{2(h_j + h_{j+1})(h_{j-1} + h_{j-2} + h_j + h_{j+1})},$$

and h_j is the distance between nodes j and $j + 1$, i.e.,

$$h_j = \sqrt{(X_{j+1} - X_j)^2 + (Z_{j+1} - Z_j)^2} \ . \tag{19}$$

Here, N is the total number of nodes on the free surface to be smoothed.

By approximating the arc length between nodes i and $i + 1$ by h_i we find the arc length of any point on the free surface of water. The corresponding X- and Z- coordinates and the potential φ near the jet are found by using Eq. (18)**.**

Matrices A and B in Eqs. (9) and (13) whose elements depend upon current coordinates of node points are evaluated after every time step. Thus we refine the mesh after every time step, and evaluate values of variables at the nodes of the new mesh from their values at the nodes of the previous mesh by using three-point spline functions, e.g., see Pozrikidis [30].

2.2.3. Numerical integration of governing equations

The fourth-order Runge-Kutta method is used to numerically integrate the system of first order ordinary differential equations included in Eq. (3.a) for X, Z and φ with $\dfrac{\partial \varphi}{\partial n}$ on the boundaries regarded as known and kept fixed. Using the notation $\Xi = \{X, Z, \varphi\}$, we write these three equations as

$$\frac{d\Xi}{dt} = f\left(\Xi, \ \frac{\partial \varphi}{\partial n}\right) \ . \tag{20}$$

The fourth-order Runge-Kutta integration method [14] gives

$$\Xi^{i+1} = \Xi^i + (k_1 + 2k_2 + 2k_3 + k_4)\delta t / 6 \ , \tag{21}$$

where

$$k_1 = f\left(\Xi^i, \ \frac{\partial \varphi^i}{\partial n}\right), \qquad k_2 = f\left(\Xi^i + k_1 \delta t/2, \ \frac{\partial \varphi^i}{\partial n}\right),$$

$$k_3 = f\left(\Xi^i + k_2 \delta t/2, \ \frac{\partial \varphi^i}{\partial n}\right), \qquad k_4 = f\left(\Xi^i + k_3 \delta t, \ \frac{\partial \varphi^i}{\partial n}\right),$$

and Ξ^i is the value of Ξ at time step i. Battistin and Iafrati [13] used one node per element and suggested that the time step size should be such that the maximum displacement of a point during a time step is less than one fourth of the corresponding element length. Here we approximate the jet tip velocity by the time derivative of $c_f(t)$ defined in Eq. (15) and select the time step size by requiring that it takes γ_t time steps for the jet tip to travel the length of one element. Thus

$$\delta t = \frac{h_{\min} \, 2\tan\beta}{V \pi \gamma_t} \tag{22}$$

where $h_{\min}$ is minimum element length near the jet tip, γ_t is assigned values between 2 and 20; here we use $\gamma_t = 5$. For the water slamming of a curved hull shown in Fig. 19, we choose β as the minimum of the local deadrise angles at nodes on the water/fluid interface, slope of the free water surface at nodes on it, and the local angle at the jet tip.

2.2.4. Analysis of hull's rigid body motion

Let $V(t)$ be the projection of the rigid body velocity $\boldsymbol{V}$ along the Z-direction and $\dot{V}(t)$ be the corresponding acceleration. The rigid body acceleration of the hull in the Z-direction is calculated from

$$\dot{V}(t) = \frac{F_Z}{M^*} - g \ , \tag{23.a}$$

$$F_Z = -M_a^* \dot{V} + F_z' \ . \tag{23.b}$$

Here M^* is the total mass of the hull, g the acceleration due to gravity, and F_Z the total upward force due to water slamming. We note that F_Z is an implicit function of the acceleration of fluid particles contacting the hull, and we decompose it into two parts; the upward force F_Z' without considering acceleration of fluid particles and $M_a^* \dot{V}$ that depends upon the acceleration of fluid particles abutting the hull. The quantity M_a^* is called the added mass since the term $M_a^* \dot{V}$ is usually transferred to the left hand side and lumped with the inertia force of the structure. Thus the net effect is equal to considering a larger mass of the structure than its true mass.

Young [31] studied the hydroelastic problem for propulsors by coupled BE and FE methods and the added mass matrix for the FE analysis of the solid body was obtained from the solution of the fluid problem by the BEM. We separate the pressure term due to fluid particles' acceleration and calculate the added mass effect for rigid body motion. It can successfully simulate the free drop test of light weight rigid wedge and rigid ship bow section.

Substituting for $\dfrac{\partial \Psi^B}{\partial n}$ from Eqs. (12.b) and (12.c) into Eq. (13) we get

$$[A]\begin{Bmatrix} \dfrac{\partial \Psi^F}{\partial n} \\ \Psi^B \\ \Psi^{T+S} \\ \\ \end{Bmatrix} = [B]\begin{Bmatrix} \Psi^F \\ -\boldsymbol{n}\cdot\dot{\boldsymbol{V}} \\ 0 \end{Bmatrix} . \tag{24}$$

With the notation

$$[\mathbb{Q}] = \begin{bmatrix} \mathbb{Q}_{11} & \mathbb{Q}_{12} & \mathbb{Q}_{13} \\ \mathbb{Q}_{21} & \mathbb{Q}_{22} & \mathbb{Q}_{23} \\ \mathbb{Q}_{31} & \mathbb{Q}_{32} & \mathbb{Q}_{33} \end{bmatrix} = [A]^{-1}[B] \ , \tag{25}$$

we write

$$\{\Psi^B\} = [\mathbb{Q}_{21}\ \mathbb{Q}_{22}\ \mathbb{Q}_{23}]\begin{Bmatrix}\Psi^F\\ -\boldsymbol{n}\cdot\dot{\boldsymbol{V}}\\ 0\end{Bmatrix} = \left\{\Psi_2^B\right\} + \left\{\Psi_1^B\right\}, \tag{26.a}$$

$$\{\Psi_2^B\} = -[\mathbb{Q}_{22}]\{\boldsymbol{n}\cdot\dot{\boldsymbol{V}}\}, \tag{26.b}$$

$$\{\Psi_1^B\} = -[\mathbb{Q}_{21}]\{\Psi^F\}. \tag{26.c}$$

It is clear from Eq. (25) that the coefficient matrix [ℚ] is derived from matrices A and B appearing in the BE formulation of the fluid problem.

By substituting in Eq. (5) for $\frac{\partial\varphi}{\partial t}$ from Eqs. (10) and (26), we get the following equations for the pressure acting on the solid/fluid interface:

$$p - p_a = -\rho\left(-\Psi^B + \boldsymbol{V}\cdot\nabla\varphi + \frac{1}{2}|\nabla\varphi|^2\right) = p_2 + p_1, \tag{27.a}$$

$$p_2 = \rho\Psi_2^B = -\rho\left[\bar{\mathbb{Q}}_{22}\right]\{n_Z\}\dot{\boldsymbol{V}}, \tag{27.b}$$

$$p_1 = -\rho\left(-\Psi_1^B + \boldsymbol{V}\cdot\nabla\varphi + \frac{1}{2}|\nabla\varphi|^2\right). \tag{27.c}$$

Here $\{n_Z\}$ is the Z-component of the unit normal to the fluid/solid interface with the unit normal pointing out of the fluid, p_2 is the pressure due to rigid body acceleration, and p_1 is the pressure without considering acceleration of the rigid body motion. The coefficient matrix $\bar{\mathbb{Q}}_{22}$ for point ƥ between nodes i and i+1 is evaluated by using the following equation:

$$\bar{\mathbb{Q}}_{22}(j) = \mathbb{Q}_{22}(i,j)\left(\frac{s_{i+1}-s}{s_{i+1}-s_i}\right) + \mathbb{Q}_{22}(i+1,j)\left(\frac{s-s_i}{s_{i+1}-s_i}\right), j = 1,\ \mathcal{N} \tag{27.d}$$

Here s, s_i and s_{i+1} are, respectively, the arc length of point ƥ, node i and node i+1, and $\mathcal{N}$ equals the number of nodes on the fluid structure interface.

We find values of a quantity at the desired location on the solid/fluid interface by either interpolating or extrapolating values at points where they are known.

Integrating component of the pressure in the Z-direction over the solid/fluid interface gives the total Z-force acting on the hull. Thus using Eq. (23.b) we get

$$F_Z = \int_0^{\ell}(p_2 + p_1)n_z\, ds = -M_a^*\dot{V} + F_z', \tag{28}$$

where

$$M_a^* = \int_0^\ell \rho n_z \left[\bar{\mathbb{Q}}_{22}\right]\{n_z\}ds, \qquad F_z' = \int_0^\ell p_1 n_z ds. \tag{29}$$

Here ℓ is the total arc length of the fluid/structure interface, and s is the arc length from the keel to a point of the hull.

Substitution from Eq. (28) into Eq. (23.a) gives

$$(M^* + M_a^*)\dot{V}(t) = F_z' - M^* g\ . \tag{30}$$

Eq. (30) is numerically integrated by using the following central-difference algorithm:

$$(M^* + M_a^*)\dot{V}^{n+1} = F_z'(t_{n+1}) - M^* g\ , \tag{31.a}$$

$$V^{n+1} = V^n + \frac{1}{2}(\dot{V}^{n+1} + \dot{V}^n)\delta t\ , \tag{31.b}$$

$$\xi^{n+1} = \xi^n - V^n \delta t - \frac{1}{2}\dot{V}^n \delta t^2\ , \tag{31.c}$$

where

$$V^{n+1} = V(t_{n+1})\,,\quad \xi^{n+1} = \xi(t_{n+1})\ . \tag{32}$$

Here ξ is the submergence of the solid body with respect to the undisturbed water surface shown in Fig. 1. The velocity and acceleration of the hull keel is assumed to be equal to the rigid body velocity and acceleration since the edge at the keel is assumed not to deform. The time step δt in Eq. (31) equals that used to integrate equations for fluid's deformations.

The flow chart for iteratively solving the fluid structure interaction (FSI) problem is given in Fig. 6. Using the known solution at time t_n, ξ^{n+1}, $\dot{V}^{n+1}$ and V^{n+1} can be evaluated by using Eq. (31). These are used to update φ and Ψ for the next iteration. The iterative process is terminated when the

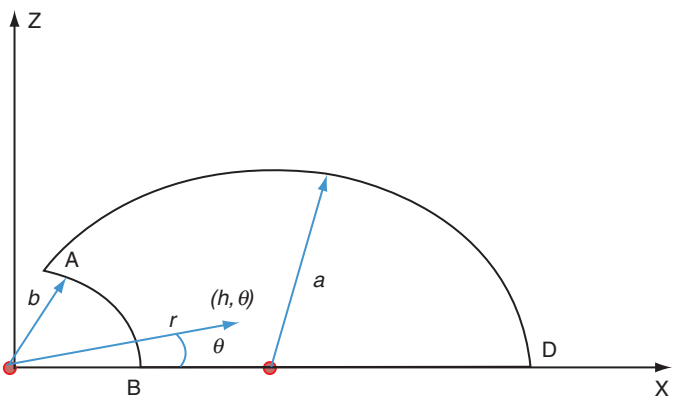

Figure 3 Domain Ω_0 for solving the Laplace equation.

normalized difference, $\int_0^{\mathcal{L}} \left| p_4^{I+1} - p_4^I \right| ds \,/\, \int_0^{\mathcal{L}} \left| p_4^{I+1} \right| ds$, of the computed total pressure between two successive iterations $I + 1$ and I is less than the prescribed tolerance of 1E-4; here $p_4 = p_1 + p_2$. The FSI procedure discussed above is called the added mass method.

2.2.5. Verification of the code

The developed BEM software has been verified by using the method of manufactured solutions (e.g., see the material just preceding and following Eq. (20) of [32]). In cylindrical coordinates, we assume that

$$\varphi = -a\left(r + \frac{b^2}{r} \right) \sin\theta, \tag{33}$$

where a and b are constants. The function φ given by Eq. (33) identically satisfies the Laplace equation. For $a = 2$ and $b = 1$, we use the software to numerically solve the Laplace equation on domain Ω_0 depicted in Fig. 3 under the following boundary conditions:

$$\varphi = 0 \text{ on } BD \,, \tag{34.a}$$

$$\frac{\partial \varphi}{\partial n} = Z \text{ on } DA \,, \tag{34.b}$$

$$\frac{\partial \varphi}{\partial n} = 0 \text{ on } AB \,. \tag{34.c}$$

The BEM software is used to find values of φ on boundaries DA and AB, and of $\frac{\partial \varphi}{\partial n}$ on boundary BD. We discretized each edge AB, BD and DA with 50 and 100 uniform elements for meshes 1 and 2, respectively, and found the difference, $\bar{\eta}$, in the computed and the analytical values of $\frac{\partial \varphi}{\partial n}$ and φ by using the following equation:

$$\bar{\eta} = \frac{\int_0^{\mathcal{L}} \left| f_{num} - f_{ana} \right| ds}{\int_0^{\mathcal{L}} \left| f_{ana} \right| ds} \,. \tag{35}$$

Here subscripts *ana* and *num* on f represent its values from the analytical and the numerical solutions, and $\mathcal{L}$ is the total arc length of the boundary.

In Figs. 4 and 5 we have compared, respectively, the analytical and the numerically computed values of the flux $\frac{\partial \varphi}{\partial n}$ on BD and of φ on the boundary $ABDA$. In each case the two curves essentially overlap each other. Values of the error norm, $\bar{\eta}$, defined by Eq. (35) and listed in Table 1 for the two meshes, are less than 0.13 %. Thus the developed BEM software gives very good solution of the Laplace equation.

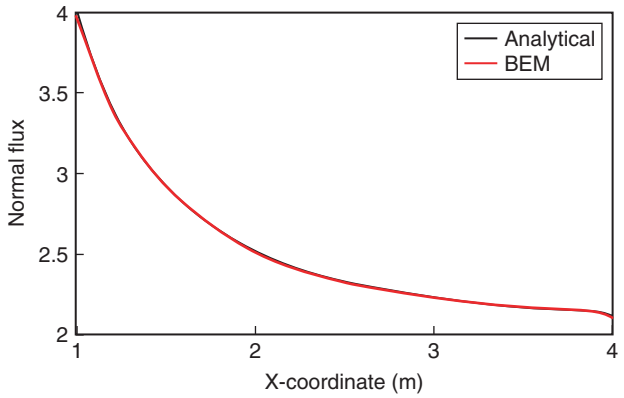

Figure 4 Comparison of variations of the analytical and the numerically computed values of $\frac{\partial \varphi}{\partial n}$ on boundary *BD*; the two curves overlap each other.

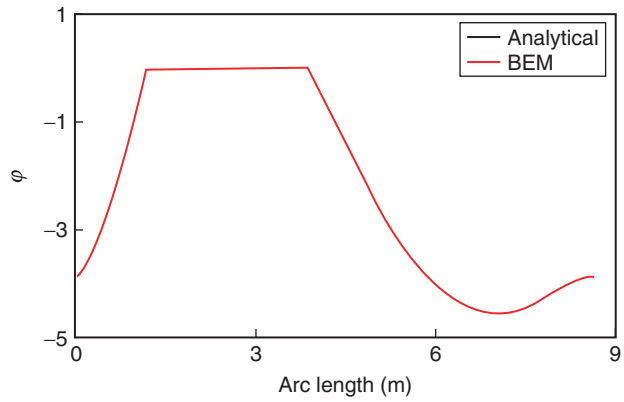

Figure 5 Comparison of variations of the analytical and the numerically computed values of φ on the boundary *ABDA* traversed counter-clockwise; the two curves overlap each other.

Table 1 For the two meshes used, values of $\bar{\eta}$ for $\frac{\partial \varphi}{\partial n}$ and φ on the boundary.

	$\frac{\partial \varphi}{\partial n}$	φ
Mesh 1	0.00122	0.000430
Mesh 2	0.000322	0.000110

3. EXAMPLE PROBLEMS

3.1. STRAIGHT WEDGE IMPACTING WATER AT UNIFORM VELOCITY

The first problem studied is that of water slamming of a straight rigid wedge moving downwards along the Z-axis with constant velocity in which we have neglected effects of the

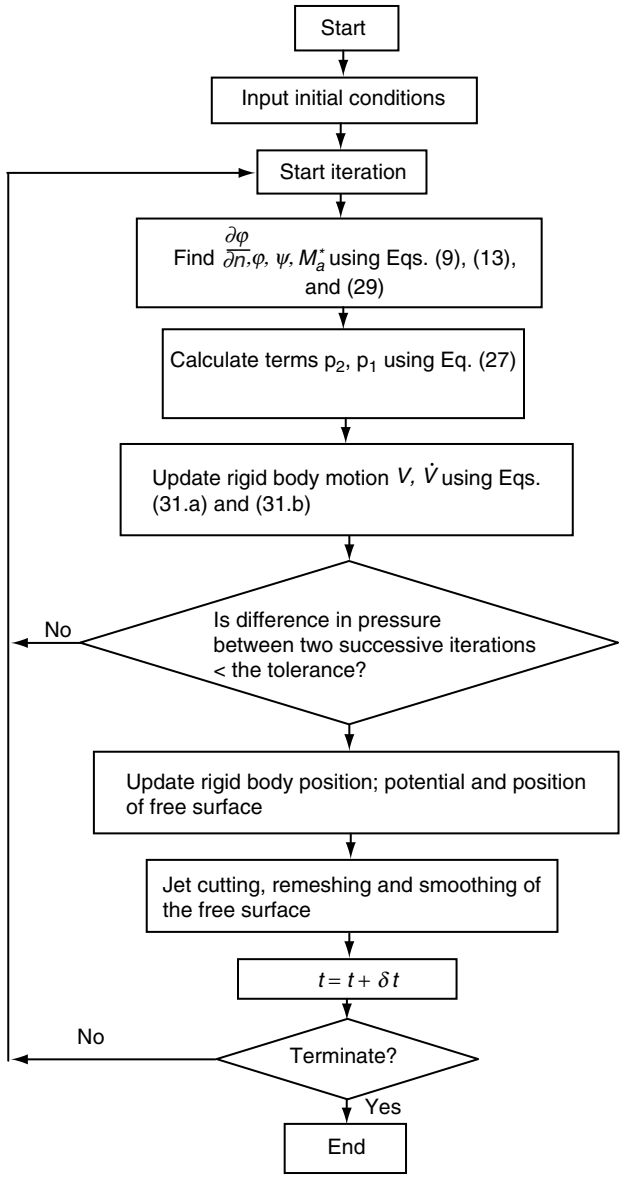

Figure 6 Flow chart of the fluid structure interaction analysis.

gravity force. The problem has been investigated, amongst others, by Zhao and Faltinsen [5] who presented a similarity solution, Sun [14] who used the BEM, Mei et al. [7] who considered the jet flow, and Das and Batra [18] who employed the commercial FE software LSDYNA. We have followed the procedure detailed in Sun's [9] dissertation; however, techniques of smoothing the free surface and truncating the jet are different from her approach.

We discretize the fluid domain boundary into two-node elements with node numbers starting from the point $\mathcal{C}$ in Fig. 7 and going counter-clockwise ($\mathcal{CDEABC}$), and denote the length of element j with nodes j and $j + 1$ by h_j. Non-uniform meshes are used to discretize

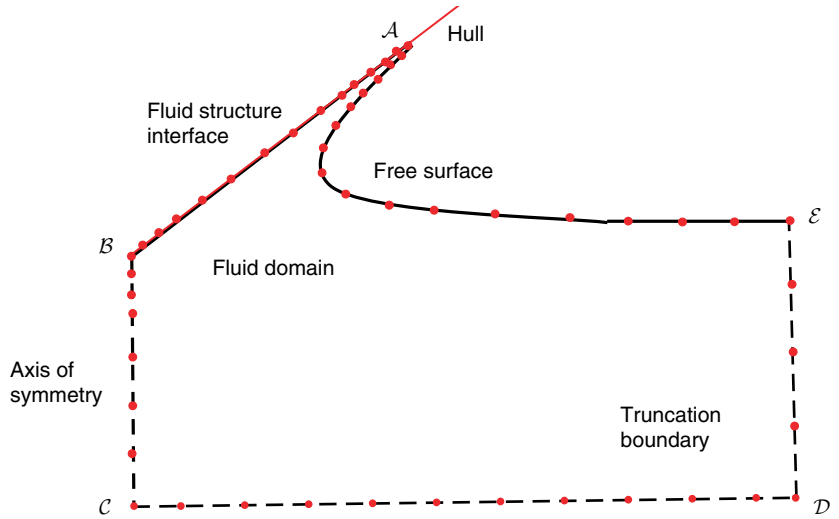

Figure 7 Regions on the fluid boundary (Not to scale).

the free surface of water near the jet tip $\mathcal{A}$, fluid boundary $\mathcal{AB}$ on the hull and also fluid boundary $\mathcal{BC}$ on the symmetry axis. In Fig. 7 the free surface of water near the wedge edge is exhibited in which points $\mathcal{A}$ and $\mathcal{B}$ are, respectively, points of intersection between the free surface and the hull, and the hull and the symmetry axis. The length, h_j, of element j for mesh 1 is chosen according to the following empirical criteria.

The length of an element on the free surface boundary $\mathcal{EA}$ is given by

$$h_j = \begin{cases} d_{34}, & \bar{N}_{\mathcal{A}} - 100 \le j < \bar{N}_{\mathcal{A}}, \\ \min(d_{33}, 1.05^{\bar{N}_{\mathcal{A}} - 100 - j} d_{34}), & j < \bar{N}_{\mathcal{A}} - 100 \text{ and } \zeta_{\mathcal{A}j} \le 1.0\mathcal{L}, \\ d_{32}, & 1.0\mathcal{L} < \zeta_{\mathcal{A}j} \le 2.0\mathcal{L}, \\ d_{31}, & \zeta_{\mathcal{A}j} > 2.0\mathcal{L}, \end{cases} \tag{36}$$

$$d_{31} = L_1/40,\ d_{32} = 1/75,\ d_{33} = d_{35}/5,\ d_{34} = d_{32}/b_r.$$

Here b_r is the mesh refinement parameter whose value depends upon the deadrise angle, $\zeta_{\mathcal{A}j}$ is the arc length between points $\mathcal{A}$ and j, and $\bar{N}_{\mathcal{A}}$ is the node number of point $\mathcal{A}$.

A non-uniform mesh with element size h_j given by Eq. (37) is used to discretize the water surface $\mathcal{AB}$ contacting the hull with finer meshes near points $\mathcal{A}$ and $\mathcal{B}$.

$$h_j = \begin{cases} d_{34}, & \bar{N}_{\mathcal{A}} \le j \le \bar{N}_{\mathcal{A}} + 100, \\ \min\left(d_{32}, 1.05^{j - (\bar{N}_{\mathcal{A}} + 100)} d_{34}\right), & j < \bar{N}_{\mathcal{A}} + 100 \text{ and } \zeta_{\mathcal{A}j} \le \zeta_{\mathcal{AB}} - 1.0\mathcal{L}, \\ 0.5 d_{32}, & j < \bar{N}_{\mathcal{A}} + 100 \text{ and } \zeta_{\mathcal{A}j} > \zeta_{\mathcal{AB}} - 1.0\mathcal{L}. \end{cases} \tag{37}$$

It is clear that this scheme generates finer meshes near points $\mathcal{A}$ and $\mathcal{B}$. The length h_j of element j on the axis of symmetry boundary $\mathcal{BC}$ is taken to be given by

$$h_j = \min\left(d_{31}, 1.2^{j-\bar{N}_B} h_{\bar{N}_B-1}\right) \tag{38}$$

Here, $\bar{N}_B$ is the node number of point $\mathcal{B}$.

The element length on each one of the two truncation boundaries $\mathcal{CD}$ and $\mathcal{DE}$ equals d_{31}. Lengths of elements for mesh 2 are the same as those for mesh 1 except that $d_{31} = L_1/80$ and $d_{32} = 1/150$; thus the element length for mesh 2 is one-half of that for mesh 1 in most of the region on the boundary. Unless otherwise specified, results presented below have been computed with mesh 2 and $b_r = 2$.

The percentage difference, $\bar{e}$, between quantities f_1 and f_2 computed with two different meshes or between the present work and that of other investigators for the same problem is defined as

$$\bar{e} = 100\frac{\int_{-1}^{\bar{Z}_{\max}} |f_1 - f_2| d\bar{Z}}{\int_{-1}^{\bar{Z}_{\max}} |f_1| d\bar{Z}} . \tag{39}$$

Here $\bar{Z} = Z/Vt, \bar{Z}_{\max} = \dfrac{c_f(t)\tan(\beta)}{Vt} - 1$, which is the maximum value at time t of $\bar{Z}$ for the wetted wedge.

We have delineated the influence of different jet cut parameters, time step size, BE mesh size and the size of the fluid domain considered on results for the water slamming of a 1 m long rigid straight wedge of different deadrise angles β impacting stationary water at uniform vertically downward velocity $V = 10$ m/s. While computing results, the time step δt is found from Eq. (22) with $\gamma_t = 5$. In an incompressible material only shear waves that do not change volume can propagate. However, here the fluid has been assumed to be inviscid implying that there are no shear waves. Thus traditional criteria for finding the time step size in the central-difference algorithm cannot be used. Problems are designated as B1, B2, and B3, respectively, for $L_1 = L_2 = 5$, 10 and 15 m, and computations are ceased when the jet tip reaches the other edge of the wedge, i.e., the entire wedge has been wetted. The variation of pressure normalized by the kinetic energy density of water moving at speed V $\left(\text{i.e., } \bar{p} = \dfrac{2p}{\rho V^2}\right)$ on the non-dimensional length of the wedge computed by different time steps and truncation boundaries is shown in Fig. 8. The percentage difference, $\bar{e}$, between pressures on the wedge computed with time steps $\delta t/2$ (used as reference for computing $\bar{e}$ in Eq. (39)) and δt is 0.2%. Results of problems B1 and B2 differ from those of problem B3 (used as reference for computing $\bar{e}$) by 1.81% and 0.286%, respectively. Unless otherwise specified, we use $L_1 = L_2 = 15$ m to analyze problems discussed below.

For rigid wedges of deadrise angles $\beta = 45°$, 30°, 10°, 4° results have been computed by taking the refinement number $b_r = 2$, 2, 10, 60, respectively, and the jet cut threshold length $\lambda_0 = 0.1\mathcal{L}$ for all four cases. In Fig. 9 we have compared the computed pressure distributions

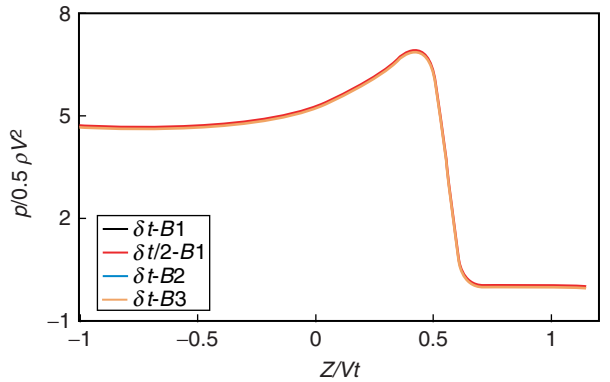

Figure 8 Distribution of the normalized slamming pressure on the wedge of deadrise angle β = 30° for different truncation boundaries and time step sizes; the four curves essentially overlap each other.

on the wedge and the water surface profiles with those reported by Sun [14] and Zhao and Faltinsen [5], and have listed values of the difference $\overline{e}$ in Table 2. The maximum difference, $\overline{e}$, between our computed pressure and that reported in [5] is 6%. Thus the pressure distributions obtained using the present technique are close to those found by Zhao and Faltinsen [5] who employed the similarity solution.

Results plotted in Fig. 9 illustrate that the deadrise angle β significantly influences the pressure distribution on the wetted hull surface. An increase in β results in more uniform distribution of pressure. The peak value of the normalized pressure (recall that the normalization pressure depends upon β) is essentially independent of β.

3.2. FREELY FALLING STRAIGHT WEDGE

We now analyze the problem studied in subsection 3.1 but consider the effect of gravitational forces acting on the wedge. The problem has been studied both analytically and numerically by Yettou et al. [8] for straight 1.2 m long wedges of different masses, entry speeds and deadrise angles; however, we study only two cases, namely that of the 94 kg wedge of deadrise angle 25°, and of 153 kg wedge of deadrise angle 30°. Each wedge enters water at 5.047 m/s. While simulating deformations, we used mesh 2 with refinement number b_r = 5, jet cut parameter = the default value, and the time step sizes are found from Eq. (22), using γ_t = 10 for each case with its corresponding deadrise angle. For $c_f(t) \le 0.005$ m,Wagner's [3] solution

$$p_w(X) = \min\left\{ \rho V \frac{c_f(t)}{\sqrt{c_f(t)^2 - X^2}} \frac{dc_f(t)}{dt}, \frac{1}{2}\rho\left(\frac{dc_f(t)}{dt}\right)^2 \right\}, X \le c_f(t), \tag{40}$$

is used to find the initial slamming pressure p_w and hence the resultant force on the wedge, and the water surface profile is computed using Eq. (14). For $c_f(t) \ge 0.005$ m, deformations of the water are analyzed by the BEM described above.

As the influence of thin jet on the total slamming pressure is negligible, we consider a wedge of length greater than 1.2 m to compute results until the 1.2 m length of the wedge completely enters the water. The presently computed time history of the Z-velocity of the

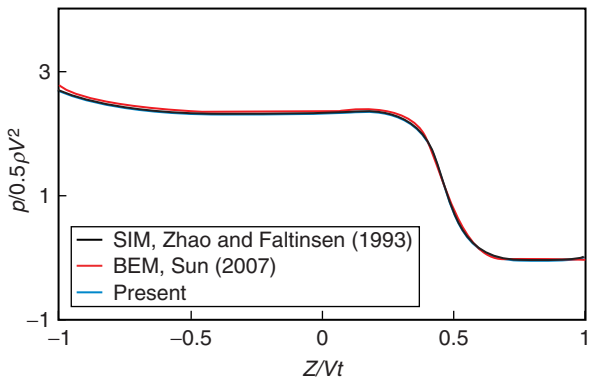

(a) Distribution of the normalized slamming pressure on the wedge of deadrise angle $\beta = 45°$

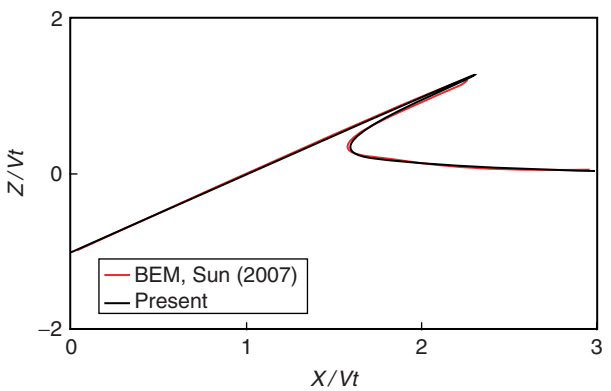

(b) Free surface of water for the rigid wedge of deadrise angle $\beta = 45°$ slamming stationary water at a uniform speed of 10 m/s.

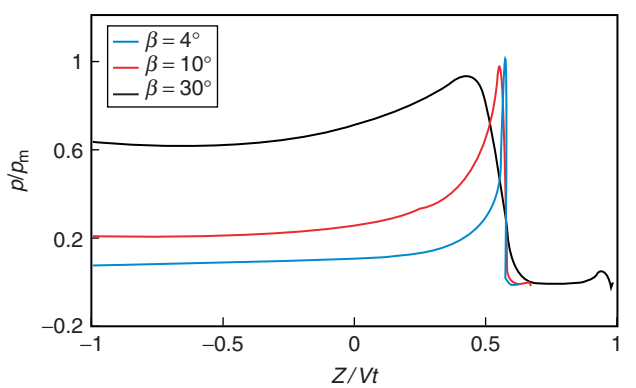

(c) Distribution of the normalized slamming pressure on the wedge for deadrise angle $\beta = 30°, 10°, 4°$; $p_m = \frac{1}{2}\rho\left(\frac{\pi v}{2tan\beta}\right)^2$.

Figure 9 (*Continued*)

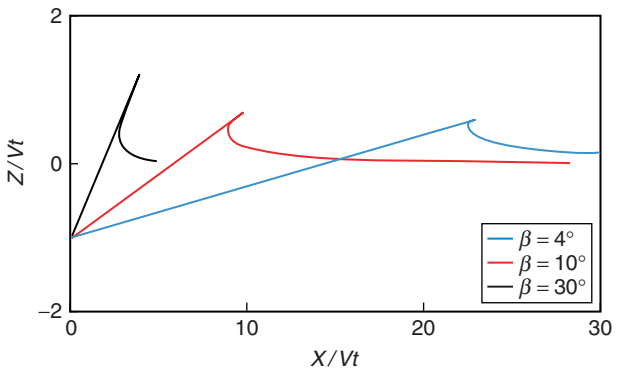

(d) Free surfaces of water for rigid wedges of deadrise angles $\beta = 30°, 10°, 4°$; slamming stationary water at the uniform speed of 10 m/s

Figure 9 Distribution of the normalized slamming pressure on the wedge and free surface of water for deadrise angles $\beta = 45°, 30°, 10°, 4°$.

Table 2 For the pressure computed on rigid straight wedge of different deadrise angles, the percentage difference $\bar{e}$ between the similarity solution of [5] and present results and those reported in [14].

Deadrise angle	**45°**	**30°**	**10°**	**4°**
BEM_Sun [14]	1.21%	3.15%	6.36%	11.6%
Present_mesh1	0.706%	1.17%	2.55%	5.94%
Present_mesh2	0.799%	1.63%	2.14%	3.09%

Table 3 Normailized peak pressure when the wetted length equals 1 m.

	Straight hull	***R* = 50 m**	***R* = 20 m**	***R* = 8 m**	***R* = 5 m**
$\frac{p^{\max}}{0.5\rho V^2}$	320	263	156	72.3	44.4

94 kg wedge is compared in Fig. 10 with that found experimentally by Yettou et al. [8], analytically by Zhao and Faltinsen [5] and numerically by Das and Batra [18] who used the commercial FE software LSDYNA. For $t \le 40$ ms, the maximum percentage differences $100\left|V^{pre} - V^{ana}\right| / V^{ana}$ and $100\left|V^{pre} - V^{\exp}\right| / V^{\exp}$ equal 3.32% and 6.89%, respectively; here V^{pre}, V^{exp} and V^{ana} denote, respectively, values of the axial velocity computed from the present work, the experimental work of [8] and the analytical solution of [5]. Thus the present approach gives good results for $t \le 40$ ms. For $t > 40$ ms, the difference between the present and the experimental values of the axial velocity increases because of possible flow separation from the wedge. The time history of the presently computed upward force acting on the wedge is compared with that of Ref. [18] in Fig. 11; the corresponding

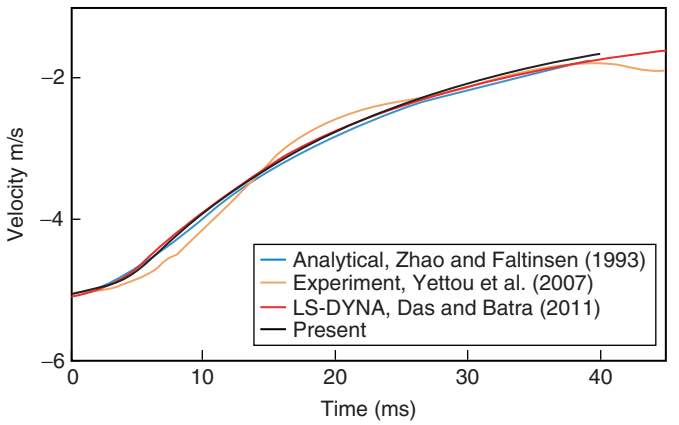

Figure 10 Time histories of the downward velocity of the 94 kg wedge.

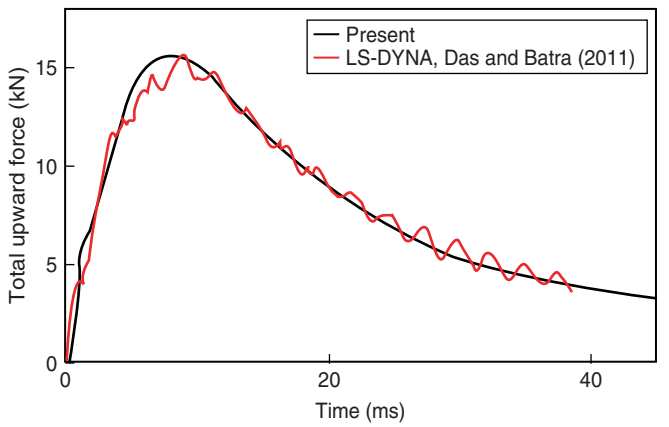

Figure 11 Time histories of the total upward force on the 94 kg wedge.

experimental results are not included in [8]. It is clear that forces acting on the rigid wedge from the two approaches are nearly the same, and the present results are smoother than those given in [18] in the sense that the amplitude of oscillations in the pressure are nearly non-existent. We note that Das and Batra [21] reported water penetrating into the rigid wedge because of the difficulty in finding values of parameters in the contact algorithm that will eliminate this interpenetration. They tried several values of these parameters and found the values that reduced oscillations in the hydrodynamic pressure acting on the wedge.

For the 153 kg wedge, the presently computed time histories of the upward total force acting on the wedge are compared with those of Yettou et al. [8] and Das and Batra [18] in Fig. 12. These evince that the present approach gives results close to those of Das and Batra [18]. Das [33] found that the total force computed by integrating the pressure reported by Yettou et al. [8] was significantly different from the value of the total upward force reported in [8]. The spatial variation of the hydrodynamic pressure on the wedge at three different times is exhibited in Fig. 13. Whereas our results agree well with those of Das and Batra, they noticeably differ from those of Yettou et al. [8]. One way to find the total upward force acting on the hull is to integrate with respect to X the pressure distribution shown in Fig. 13a

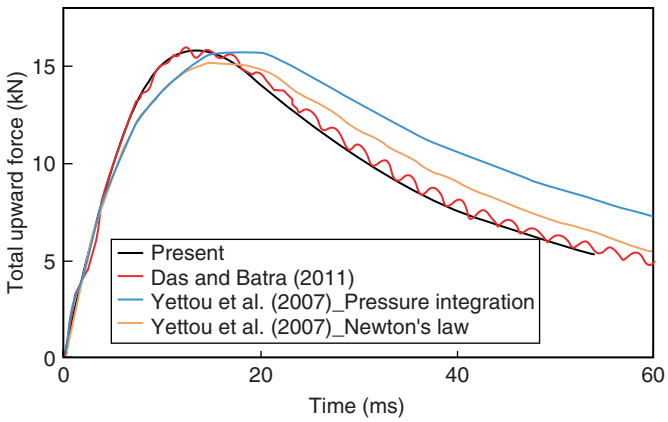

Figure 12 Time histories of the upward force on the 153 kg wedge.

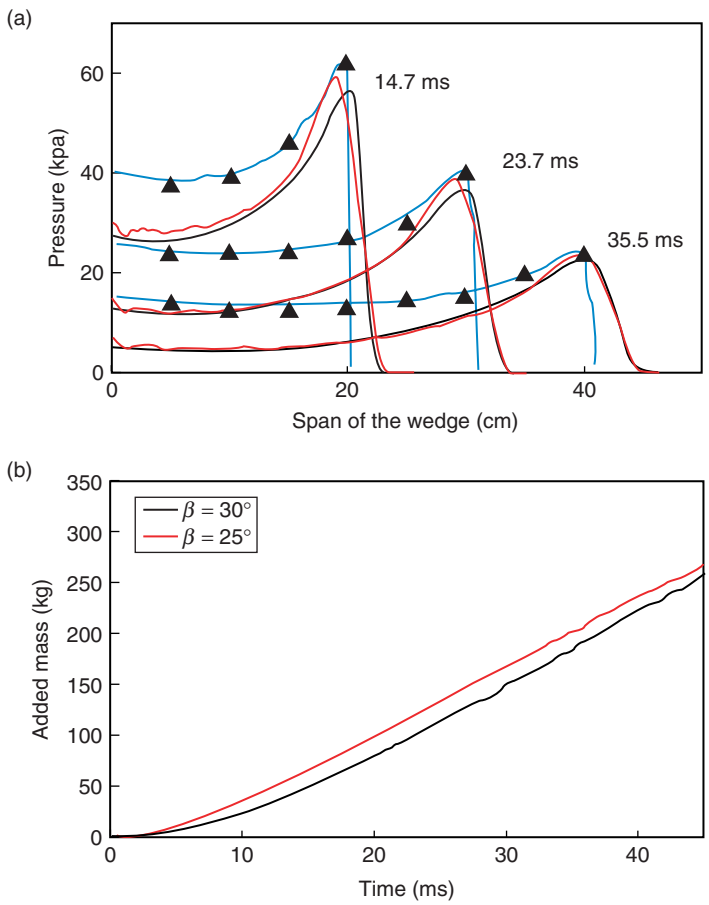

Figure 13 (a) Variations of the slamming pressure on the 153 kg rigid wedge at three different times; blue lines and solid black triangles represent, respectively, analytical and experimental results of Yettou et al. [8]; black solid and red solid curves represent, respectively, present results and those of Das and Batra [18], (b) Time histories of the added mass matrix for the wedges of deadrise angles 25° and 30°.

and multiply it with the wetted length and cos(30°). The axial force so found from Yettou et al.'s [8] pressure distribution differs from their values exhibited in Fig. 10 by 19.0%, 18.8% and 15.3% for time t = 14.7, 23.7 and 35.5 ms, respectively. However, the difference, $100\left|F^{Das} - F^{Pre}\right| / F^{Das}$, between the present total upward force F^{Pre} and the total upward force F^{Das} computed using LSDYNA by Das and Batra [18] equals 3.80%, 1.35% and 1.49% for time t = 14.7, 23.7 and 35.5 ms, respectively. Time histories of the added mass M_a^* for the two hulls of masse 94 kg (wedge of deadrise angle 25°), and of 153 kg (wedge of deadrise angle 30°) are exhibited in Fig. 13b. It is clear that the added mass does not depend upon the wedge mass but on the mass of the water displaced and the average acceleration of this body of displaced water.

3.3. FREELY FALLING BOW SECTION

The drop test into stationary water of ship bow section conducted by Aarsnes [34] has been simulated in this section and computed results have been compared with experimental findings of Aarsnes [34] and numerical results reported in Sun [14]. The shape of the ship bow section of total length 1 m and weight 261 kg is shown in Fig 14. The roll angle equals 0, and the initial entry velocity is 2.43 m/s. The initial time is assumed to be 0 ms. As the total upward force is small for t < 0.1 ms, the slamming pressure is assumed to be zero for t < 0.1 ms. While simulating deformations, we used mesh 2 with refinement number b_r = 4, jet cut parameter = the default value, and the time step size is found from Eq. (22) with β = 30°, γ_t = 10 and V = 2.43 m/s. We note that the local deadrise angle varies along the length of the bow section and is greater than 30° except for points near the hull apex P1. Because the ship bow profile between two adjacent nodes is approximated by a straight line, the pressure distribution on it may exhibit oscillations as pointed out by Sun [9].

Time histories of the total upward force and the Z-velocity plotted in Figs. 15 and 16 evince that our computed results are close to those of Sun [14] and also to the experimental findings of Aarsnes. Reasons for the difference between the computed and the experimental results include errors in approximating the ship bow section profile, 3-D effects not considered in the 2-D simulations, neglecting effects of the fluid viscosity, surface tension and gravity, and assuming fluid deformations to be irrotational.

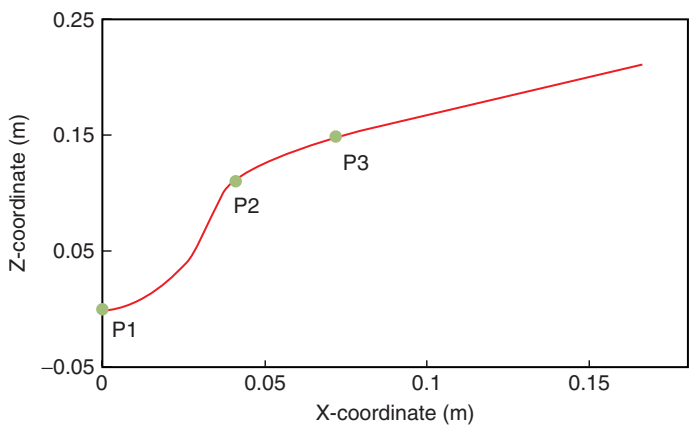

Figure 14 Cross section of the ship bow studied.

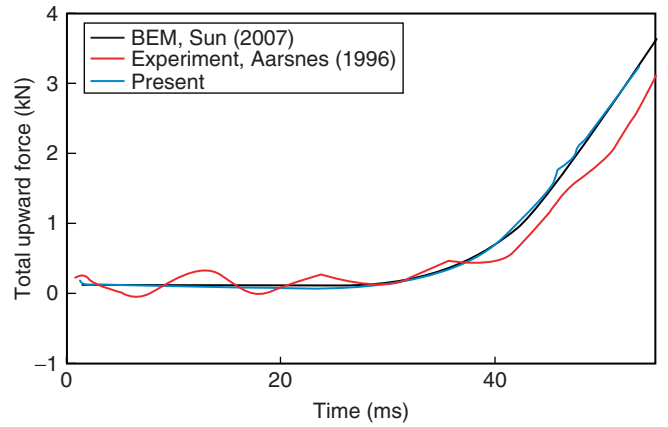

Figure 15 Time histories of the total upward force for the rigid ship bow section.

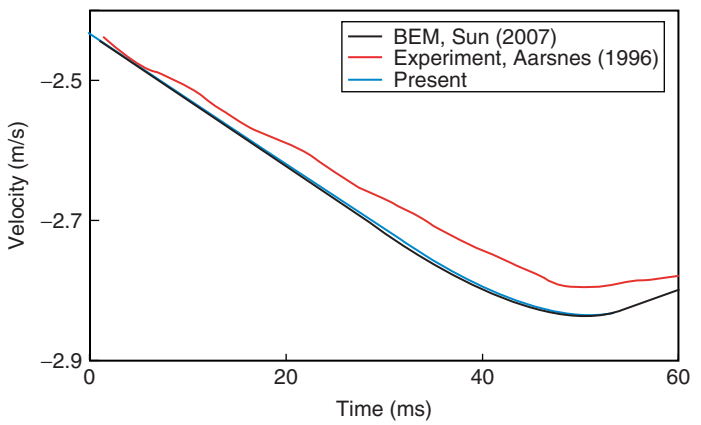

Figure 16 Time histories of the Z-velocity of the rigid ship bow section.

Time histories of the pressure at points P1 (0, 0), P2 (0.041, 0.111) and P3 (0.072, 0.149) are exhibited in Fig. 17a, b, c, those of the added mass in Fig. 17d, and the spatial variations of the pressure on the ship bow section at time t = 20.6 ms, 29.6 ms, 37.2 ms, 44.8 ms and 50.8 ms are plotted in Fig. 18. It is clear that the pressure distributions on the ship bow section are quite different from those on the straight wedge section. For the straight wedge, the high pressure region is narrow and distributed near the jet flow while that for the ship bow section the high pressure region is quite broad as also reported by Arai and Matsunaga [35]. The maximum added mass of 15 kg is much less than 261 kg weight of the ship bow section.

3.4. CIRCULAR HULL

In an attempt to delineate effects of local hull curvature on the hydrodynamic pressure acting on the hull, we consider hulls of different radii and off-set their centers so as to have an initial deadrise angle of 5°; e.g., see Fig. 19. We assume uniform entry velocity of 10 m/s and arc length of the hull is equal to 1 m. We use mesh 2 with refinement number b_r = 30, jet cut

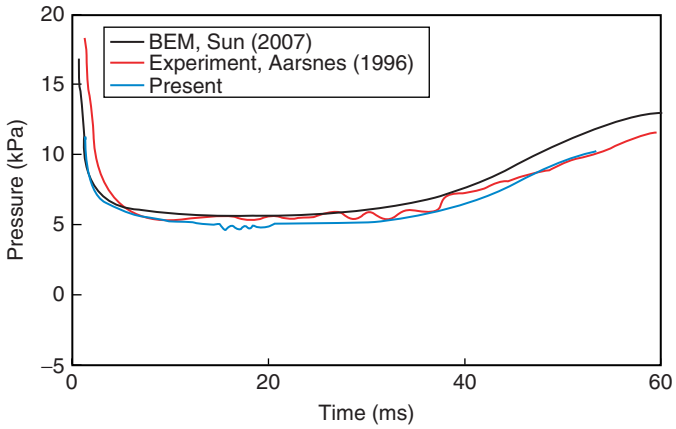

(a) Time histories of the slamming pressure at point P1.

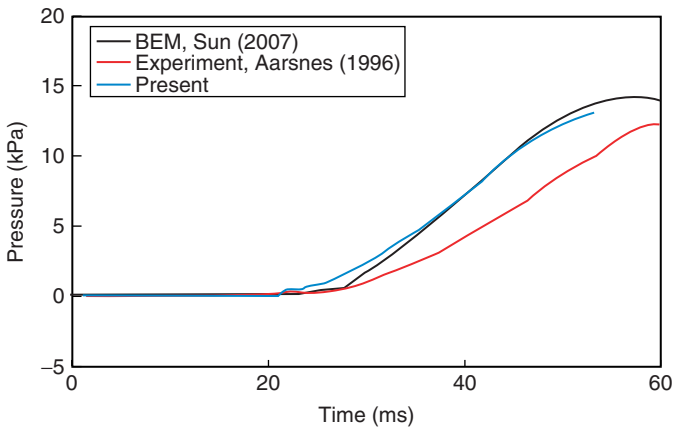

(b) Time histories of the slamming pressure at point P2.

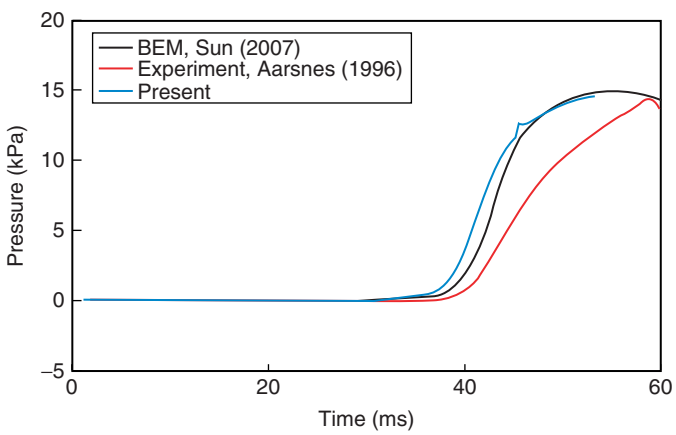

(c) Time histories of the slamming pressure at point P3.

Figure 17 (*Continued*)

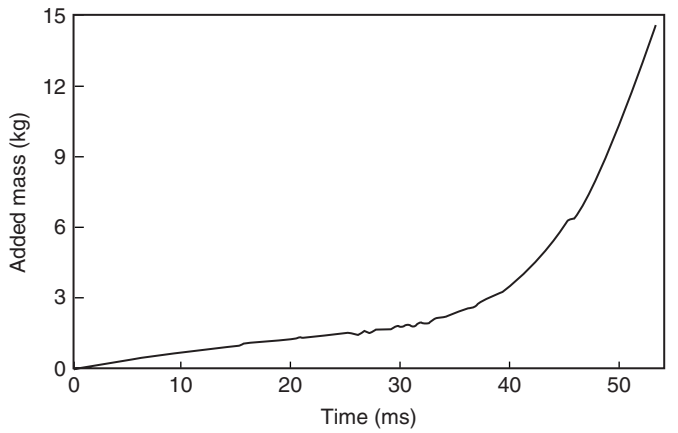

(d) Time history of the added mass

Figure 17 Time histories of the slamming pressure at points P1, P2 and P3, and time history of the added mass.

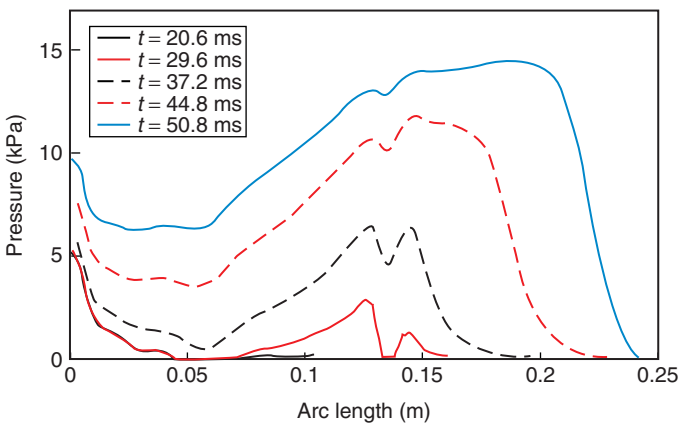

Figure 18 Variations of the pressure on the ship bow section at times t = 20.6 ms, 29.6 ms, 37.2 ms, 44.8 ms, and 50.8 ms.

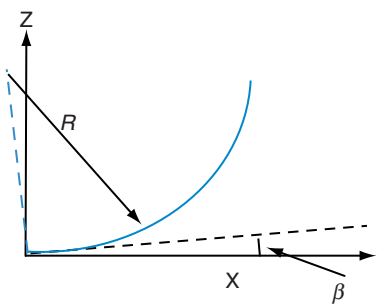

Figure 19 Sketch of circular hull and the definition of deadrise angle at $X = Z = 0$.

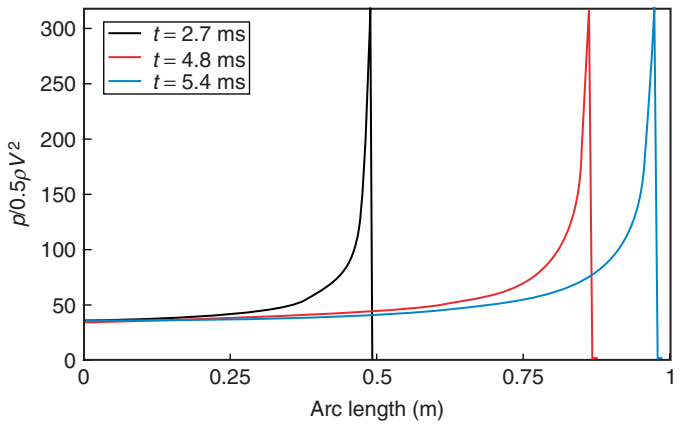

(a) Straight hull ($\beta = 5°$)

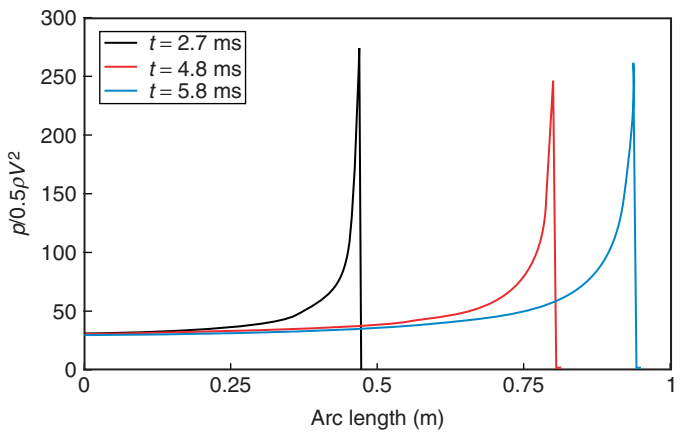

(b) $R = 50$ m

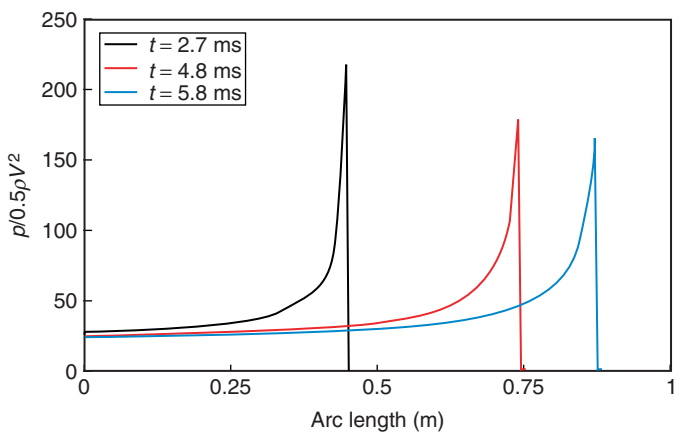

(c) $R = 20$ m

Figure 20 (*Continued*)

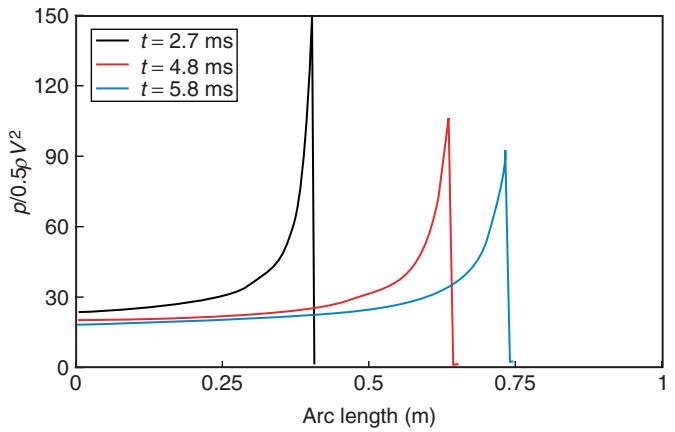

(d) $R = 8$ m

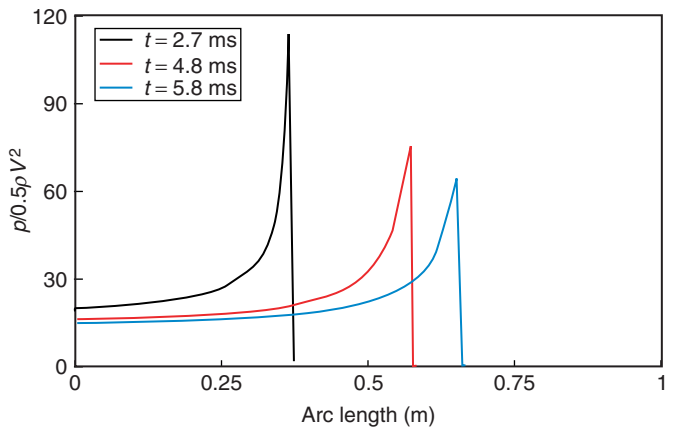

(e) $R = 5$ m

Figure 20 Variation of pressure on the rigid circular hulls of different radii.

parameter = the default value, and the time step size is found from Eq. (22) with $\beta = 5°$, $\gamma_t = 10$. For $R = 5$, 8, 20 and 50 m, we have exhibited in Fig. 20 the variation of the hydrodynamic pressure on curved and straight hulls at $t = 2.7$, 4.8 and 5.4 ms after the hull contacts stationary water. Hull's velocity is assumed to be constant and equal 10 m/s. For comparison purposes, we have also plotted the pressure distribution on a straight hull of deadrise angle = 5°. It is clear that the curvature of the hull noticeably affects the magnitude of the peak pressure and the pressure distribution on the hull. Whereas for a straight hull the peak pressure stays constant as the wetted length increases, for the curved hull the peak pressure decreases with an increase in the wetted length. In each case the peak pressure occurs near the terminus of the wetted length.

The time history of the wetted arc length is exhibited in Fig. 21. If we interpret the slope of these curves as the speed of the wetted arc length terminus, then this speed slowly decreases with an increase in the arc length.

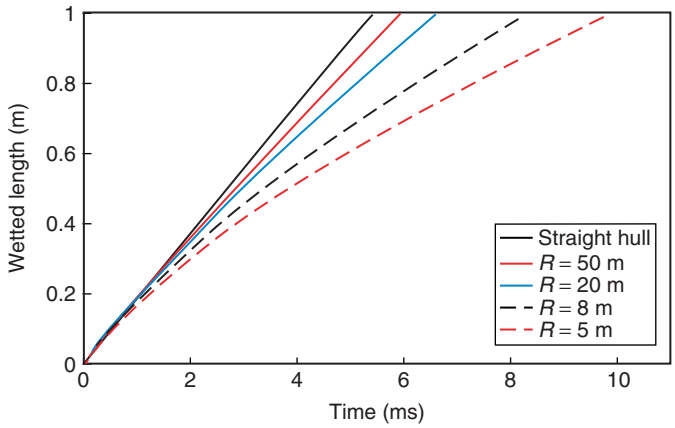

Figure 21 Time history of wetted length for rigid circular hulls of different radii.

For circular hull of radius 20 m, we have exhibited in Fig. 22 the velocity potential and stream lines in the region near the water jet, and the tangential velocity of water on the hull surface. It is clear that the tangential velocity of water near the end of the wetted length sharply increases.

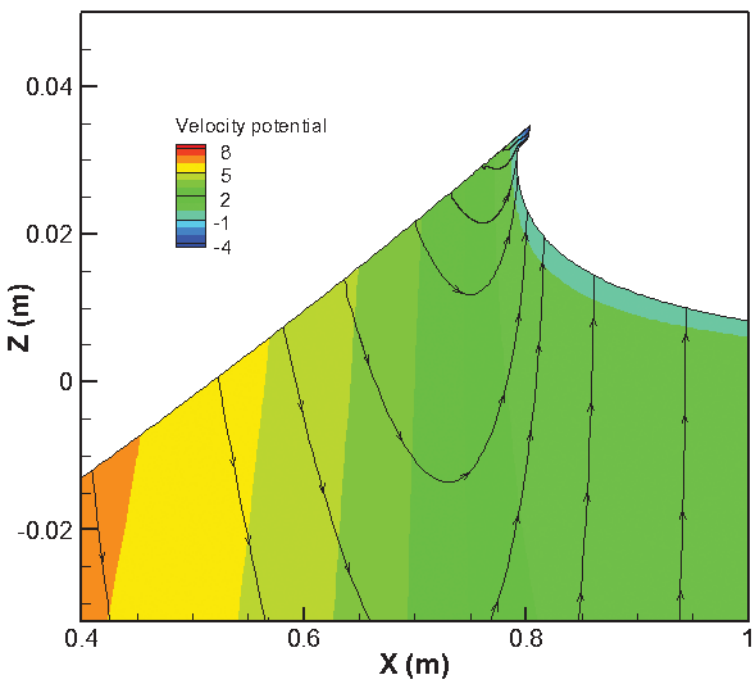

Figure 22. contunued over

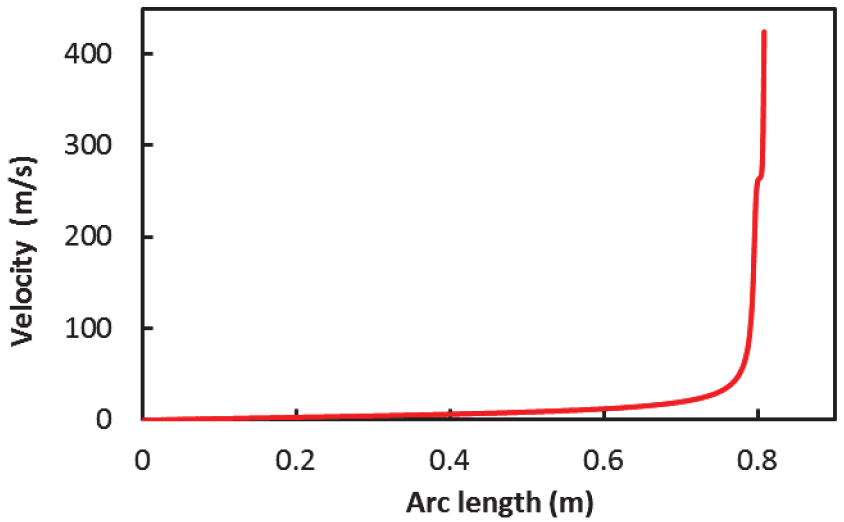

Figure 22 At t = 5.2 ms, for water slamming of the rigid circular hull of radius R=20 m, velocity potential and streamlines (top) and variation of tangential velocity of fluid particles contacting the hull (bottom).

4. CONCLUSIONS

We have used the boundary element method to analyze transient 2-dimensional deformations of homogeneous, incompressible and inviscid water assumed to undergo irrotational deformations. The velocity potential is a solution of the Laplace equation defined on the fluid domain. Strategies to determine the evolution of free surface of water and the wetted length of a hull that impacts initially stationary water have been developed. The developed code has been verified by the method of manufactured solutions. Four initial-boundary-value problems involving water slamming of straight wedge with and without considering gravitational effects on the wedge, a ship bow section, and circular hulls have been studied. For the first three problems, the pressure distribution on the wetted length and shapes of water jets near the edge of the wetted length have been found to compare well with either the experimental or the analytical or the numerical results of other investigators. For circular and straight hulls the pressure distribution on the hull can be viewed as a pressure wave traveling along the hull; the peak pressure in the wave occurs at its leading edge which is close to the terminus of the wetted length and the pressure distribution is uniform in its wake.

ACKNOWLEDGEMENTS

This work was supported by the US Office of Naval Research grant N00014-11-1-0594 to Virginia Polytechnic Institute and State University with Dr. Y.D.S. Rajapakse as the program manager; this support is gratefully acknowledged. Views expressed in the paper are those of authors and neither of the funding agency nor of authors' Institution.

REFERENCES

[1] Faltinsen, O.M., *Sea loads on ships and offshore structures*. Vol. 1. 1993: Cambridge Univ Pr.

[2] Von Karman, T., *The impact on seaplane floats during landing*. NASA, 1929(TN-321).

[3] Wagner, H., *Über Stoβ - und Gleitvorgänge an der Oberfläche von Flüssigkeiten*. ZAMM-Journal of Applied Mathematics and Mechanics/Zeitschrift für Angewandte Mathematik und Mechanik, 1932. **12**(4): p. 193–215.

[4] Dobrovol'Skaya, Z., *On some problems of similarity flow of fluid with a free surface*. Journal of Fluid Mechanics, 1969. **36**(04): p. 805–829.

[5] Zhao, R. and O. Faltinsen, *Water entry of two-dimensional bodies*. Journal of Fluid Mechanics, 1993. **246**(1): p. 593–612.

[6] Zhao, R., O. Faltinsen, and J. Aarsnes. *Water entry of arbitrary two-dimensional sections with and without flow separation*. in *Twenty-first Symposium on NAVAL HYDRODYNAMICS*. 1996.

[7] Mei, X., Y. Liu, and D.K.P. Yue, *On the water impact of general two-dimensional sections*. Applied Ocean Research, 1999. **21**(1): p. 1–15.

[8] Yettou, E.M., A. Desrochers, and Y. Champoux, *A new analytical model for pressure estimation of symmetrical water impact of a rigid wedge at variable velocities*. Journal of fluids and structures, 2007. **23**(3): p. 501–522.

[9] Donguy, B., B. Peseux, L. Gornet, and E. Fontaine. *Three-dimensional hydroelastic water entry: preliminary results*. in *International Offshore and Polar Engineering Conference*. 2001. Stavanger, Norway.

[10] Stenius, I., A. Rosén, and J. Kuttenkeuler, *Explicit FE-modelling of fluid-structure interaction in hull-water impacts*. International Shipbuilding Progress, 2006. **53**(2): p. 103–121.

[11] Oger, G., M. Doring, B. Alessandrini, and P. Ferrant, *Two-dimensional SPH simulations of wedge water entries*. Journal of Computational Physics, 2006. **213**(2): p. 803–822.

[12] Lin, M. and T. Ho, *Water-entry for a wedge in arbitrary water depth*. Engineering analysis with boundary elements, 1994. **14**(2): p. 179–185.

[13] Battistin, D. and A. Iafrati, *Hydrodynamic loads during water entry of two-dimensional and axisymmetric bodies*. Journal of fluids and structures, 2003. **17**(5): p. 643–664.

[14] Sun, H., *A Boundary Element Method applied to strongly nonlinear wave-body interaction problems*, 2007, Trondheim: Norwegian University of Science and Technology.

[15] Sun, H. and O.M. Faltinsen, *Water impact of horizontal circular cylinders and cylindrical shells*. Applied Ocean Research, 2006. **28**(5): p. 299–311.

[16] Sun, H. and O.M. Faltinsen, *Water entry of a bow-flare ship section with roll angle*. Journal of Marine Science and Technology, 2009. **14**(1): p. 69–79.

[17] Qin, Z. and R. Batra, *Local slamming impact of sandwich composite hulls*. International Journal of Solids and Structures, 2009. **46**(10): p. 2011–2035.

[18] Das, K. and R.C. Batra, *Local water slamming impact on sandwich composite hulls*. Journal of fluids and structures, 2011. **27**(4): p. 523–551.

[19] Stenius, I., A. Rosén, and J. Kuttenkeuler, *Hydroelastic interaction in panel-water impacts of high-speed craft*. Ocean Engineering, 2010. **38**(2–3): p. 371–381.

[20] Lu, C., Y. He, and G. Wu, *Coupled analysis of nonlinear interaction between fluid and structure during impact*. Journal of fluids and structures, 2000. **14**(1): p. 127–146.

[21] Panciroli, R., S. Abrate, G. Minak, and A. Zucchelli, *Hydroelasticity in water-entry problems: Comparison between experimental and SPH results*. Composite Structures, 2011.

[22] Charca, S., B. Shafiq, and F. Just, *Repeated slamming of sandwich composite panels on water.* Journal of Sandwich Structures and Materials, 2009. **11**: p. 409–424.

[23] Charca, S. and B. Shafiq, *Damage assessment due to single slamming of foam core sandwich composites*. Journal of Sandwich Structures and Materials, 2010. **12**: p. 97–112.

[24] Hu, Z.H., X.D. He, J. Shi, R.G. Wang, and H.J. Liu, *Study on Delamination Problems of Composite Hull Structures under Slamming Loads*. Polymers & Polymer Composites, 2011. **19**(4–5): p. 433–437.

[25] Van Paepegem, W., C. Blommaert, I. De Baere, J. Degrieck, G. De Backer, J. De Rouck, J. Degroote, J. Vierendeels, S. Matthys, and L. Taerwe, *Slamming wave impact of a composite buoy for wave energy applications: Design and large - scale testing*. Polymer Composites, 2011. **32**(5): p. 700–713.

[26] Aureli, M., C. Prince, M. Porfiri, and S.D. Peterson, *Energy harvesting from base excitation of ionic polymer metal composites in fluid environments*. Smart Materials and Structures, 2010. **19**: p. 015003.

[27] París, F. and J. Cañas *Boundary element method: fundamentals and applications* 1997: Oxford University Press New York.

[28] Greco, M., *A two-dimensional study of green-water loading*, 2001, Norwegian University of Science and Technology.

[29] Longuet-Higgins, M.S. and E. Cokelet, *The deformation of steep surface waves on water. I. A numerical method of computation*. Proceedings of the Royal Society of London. A. Mathematical and Physical Sciences, 1976. **350**(1660): p. 1–26.

[30] Pozrikidis, C., *Numerical computation in science and engineering* 1998: Oxford University Press London.

[31] Young, Y., *Time-dependent hydroelastic analysis of cavitating propulsors*. Journal of fluids and structures, 2007. **23**(2): p. 269–295.

[32] Batra, R. and X. Liang, *Finite dynamic deformations of smart structures*. Computational mechanics, 1997. **20**(5): p. 427–438.

[33] Das, K., *Analysis of instabilities in microelectromechanical systems, and of local water slamming*, 2009, Ph.D. dissertation, Virginia Polytechnic Institute and State University.

[34] Aarsnes, J., *Drop test with ship sections–effect of roll angle*. Marintek report, 1996. **603834**(01).

[35] Arai, M. and K. Matsunaga, *A numerical and experimental study of bow flare slamming*. Journal of the Society of Naval Architects of Japan, 1989. **166**: p. 343–353.

APPENDIX: BOUNDARY CONDITIONS ON Ψ

The auxiliary function Ψ and operator $\frac{D_B}{Dt}$ can be defined as

$$\Psi = \frac{D_B \varphi}{Dt} = \frac{\partial \varphi}{\partial t} + \boldsymbol{V} \cdot \nabla \varphi \ , \tag{A.1.a}$$

$$\frac{D_B}{Dt} = \frac{\partial}{\partial t} + \boldsymbol{V} \cdot \nabla \ . \tag{A.1.b}$$

As the fluid is assumed to be incompressible and its deformations irrotational, and $\boldsymbol{V}$ equals the translational velocity of a rigid body (no rotation), we have the following equations.

$$\nabla^2 \varphi = 0 \, , \tag{A.2.a}$$

$$\nabla \times \nabla\varphi = \mathbf{0}\,, \tag{A.2.b}$$

$$\nabla \cdot \boldsymbol{V} = 0, \tag{A.2.c}$$

$$\nabla \times \boldsymbol{V} = \mathbf{0}\,. \tag{C.2.d}$$

Applying the Laplace operator to Bernoulli's Eq. (5), we get

$$-\nabla^2\left(\frac{\partial\varphi}{\partial t} + \boldsymbol{V}\cdot\nabla\varphi\right) + \nabla^2(\boldsymbol{V}\cdot\nabla\varphi) + \nabla^2\left(\frac{1}{2}\left|\nabla\varphi\right|^2 + \frac{p-p_a}{\rho}\right) = 0\,. \tag{A.3.a}$$

We note that

$$\nabla^2(\boldsymbol{V}\cdot\nabla\varphi) = \boldsymbol{V}\cdot\nabla(\nabla^2\varphi) = 0\,, \tag{A.3.b}$$

$$\nabla^2\left(\frac{1}{2}\left|\nabla\varphi\right|^2 + \frac{p-p_a}{\rho}\right) = \nabla\cdot\left(\nabla\varphi\cdot\nabla\nabla\varphi + \nabla\frac{p-p_a}{\rho}\right) = \nabla\cdot\left(\frac{\partial\nabla\varphi}{\partial t}\right) = 0\,. \tag{A.3.c}$$

Applying the Laplace operator to Eq. (A.1.a) and using Eq. (A.3), we obtain

$$\nabla^2\Psi = \nabla^2\left(\frac{\partial\varphi}{\partial t} + \boldsymbol{V}\cdot\nabla\varphi\right) = 0\,. \tag{A.4}$$

In order to prove the relation

$$\frac{\partial\Psi}{\partial n} = \frac{\partial}{\partial n}\left(\frac{D_B\varphi}{Dt}\right) = \frac{D_B}{Dt}\left(\frac{\partial\varphi}{\partial n}\right), \tag{A.5}$$

we assume that $\dfrac{D_B}{Dt}(\boldsymbol{n})$ is small, and note that

$$\begin{aligned}\frac{D_B}{Dt}\left(\frac{\partial\varphi}{\partial n}\right) &= \boldsymbol{n}\cdot\left(\frac{\partial\nabla\varphi}{\partial t} + \boldsymbol{V}.\nabla\nabla\varphi\right) = \boldsymbol{n}\cdot\left(\frac{\partial\nabla\varphi}{\partial t} + \nabla(\boldsymbol{V}\cdot\nabla\varphi)\right),\\ &= \boldsymbol{n}\cdot\nabla\left(\frac{\partial\varphi}{\partial t} + \boldsymbol{V}\cdot\nabla\varphi\right) = \frac{\partial}{\partial n}\left(\frac{D_B\varphi}{Dt}\right).\end{aligned} \tag{A.6}$$

Substituting from Eq. (2) into Eq. (A.5), the boundary condition on the solid body is given by

$$\frac{\partial\Psi}{\partial n} = \frac{D_B}{Dt}\left(\frac{\partial\varphi}{\partial n}\right) = \frac{D_B}{Dt}(-\boldsymbol{V}\cdot\boldsymbol{n}) = -\dot{\boldsymbol{V}}\cdot\boldsymbol{n}\,. \tag{A.7}$$

The boundary condition of zero normal velocity of the fluid on the symmetry axis and the truncation boundaries requires that

$$\frac{\partial \Psi}{\partial n} = \frac{D_B}{Dt}\left(\frac{\partial \varphi}{\partial n}\right) = 0 \ . \tag{A.8}$$

Substituting from Eq. (A.1.a) into Eq. (5), the boundary condition on the free surface can be written as

$$\Psi = \frac{\partial \varphi}{\partial t} + \boldsymbol{V}\cdot\nabla\varphi = -\left(-\frac{\partial \varphi}{\partial t} + \frac{1}{2}\left|\nabla\varphi\right|^2\right) + \boldsymbol{V}\cdot\nabla\varphi + \frac{1}{2}\left|\nabla\varphi\right|^2 = \boldsymbol{V}\cdot\nabla\varphi + \frac{1}{2}\left|\nabla\varphi\right|^2 \ . \tag{A.9}$$